
Performance of Multiplexed Ge:Ga Detector Arrays in the Far Infrared

Jam Farhoomand and Craig McCreight

October 1990

(NASA-TM-102275) PERFORMANCE OF MULTIPLEXED
Ge:Ga DETECTOR ARRAYS IN THE FAR INFRARED
(NASA) 26 p CSCL 038

N91-14087

Unclass
63/88 0321132



National Aeronautics and
Space Administration

1

2

3

4

5

6

7

8

Performance of Multiplexed GE:GA Detector Arrays in the Far Infrared

Jam Farhoomand, Sterling Federal Systems, Inc., Palo Alto, California
Craig McCreight, Ames Research Center, Moffett Field, California

October 1990



National Aeronautics and
Space Administration

Ames Research Center
Moffett Field, California 94035-1000

PERFORMANCE OF MULTIPLEXED GE:GA DETECTOR ARRAYS IN THE FAR INFRARED

Jam Farhoomand* and Craig McCreight

Ames Research Center

SUMMARY

The performance of two multielement, multiplexed Ge:Ga linear arrays under low-background conditions has been investigated. The on-focal-plane switching is accomplished by MOSFET switches, and the integrated charge is made available through MOSFET source followers. The tests were conducted at $106\text{ }\mu\text{m}$, and the radiation on the detectors was confined to a spectral window $1.25\text{ }\mu\text{m}$ wide using a stack of cold filters. At 4.2 K, the highest responsivity was 584 A/W , the noise equivalent power was $1.0 \times 10^{-16}\text{ W}/\sqrt{\text{Hz}}$, and the read noise was 6100 electrons/sample. A detailed description of the test setup and procedure is presented.

INTRODUCTION

The development of infrared detector arrays with focal-plane electronics and multiplexed circuitry has enjoyed a major thrust in the past several years. The advantages of these systems for low-background astronomy have been studied in detail and have been demonstrated in laboratory and field observations. For an early demonstration of this concept, one may refer to the results obtained by the successful Infrared Astronomical Satellite (IRAS) mission which used 62 discrete detectors in its focal plane. A recent evaluation of Si:Sb and Si:Ga 58×62 -element arrays in the spectral range of 4 to $31\text{ }\mu\text{m}$ showed substantial improvements in responsivity, read noise, and dark current, making these arrays even more attractive for low-background observations (ref. 1).

The future projects for space-based observatories such as the Space Infrared Telescope Facility (SIRTF) (ref. 2) and the Large Deployable Reflector (LDR) (ref. 3), however, introduce new challenges to the development of integrated arrays. With the entire spectral window, from near-infrared to millimeter waves, open for astronomical studies, it has become imperative to extend state-of-the-art integrated detector technology to the longer wavelength regions. In recent years, progress has been made in developing discrete far-infrared and submillimeter detectors, such as extrinsic germanium (refs. 4-7) and gallium arsenide (ref. 8) photoconductors, which have achieved or show promise of achieving background-limited performance in the near future. The progress in discrete detector technology in this region has paved the way for the development of integrated far-infrared detector arrays.

*Sterling Federal Systems, Inc., Palo Alto, CA.

As part of the continuing effort at this laboratory to bring state-of-the-art detector technology to the astronomy community, we have studied the performance of two multielement, multiplexed Ge:Ga detector arrays at 106 μm . Module 01 is a 1×4 -element detector array with discrete MOSFETs, and Module 02 is a 1×2 -element array with discrete unit cells but with integrated MOSFETs for each cell. The arrays and their support electronics were developed by Aerojet ElectroSystems Company (ref. 9). The fundamental parameters of each array, such as responsivity and noise, were measured under low-background conditions.

The authors would like to thank Herb Pickett for allowing the use of his laboratory facilities and Manfred Birk, Dean Peterson, and Tim Crawford for their help in measuring the spectral transmission of our Fabry-Perots on the Bruker interferometer at the Jet Propulsion Laboratory.

OPTICAL LAYOUT

The optical configuration of the detector system is shown in figure 1. The detector assembly is placed on the cold plate of a bottom-looking He-cooled Dewar (Model HD3-8, Infrared Laboratories). The window to the outside is blanked off and an internal blackbody is used to provide the calibrated radiation on the detector.

The blackbody is an oxygen-free copper cylinder about 1 in. in diameter and 2 in. in length. To provide unit emissivity, the cylinder is painted on the inside with infrared-absorbing black paint (Ames 24E) (ref. 10). The absorption of this paint was found to be better than 99% in the spectral range from 25 to 200 μm . The output aperture of the cylinder is about 0.2 in. in diameter. This aperture, however, is not the limiting aperture of the system. The 0.004-in. manganin wire wrapped around the outside of the cylinder provides the means to heat the cylinder to the desired temperature. A calibrated silicon diode (DT 500, Lakeshore Cryotronics) and a calibrated carbon resistor placed on the top, opposite the output aperture, monitor the (absolute) blackbody temperature to within ± 0.6 K in the range of 1.4 K to 80 K. The cylinder is suspended inside a black-painted cavity by a stainless steel hypodermic needle. Two stainless steel 2-56 screws provide additional thermal paths from the inside cylinder to the outside cold environment. The screws are torqued so that a convenient thermal time-constant is obtained without introducing an excessive heat load on the He bath. The blackbody is attached to the top of the 4.2-K aluminum baffle box covering the detector array.

Immediately below the blackbody is a copper disk with a 0.100-in. hole at its center. This aperture is the cold-limiting aperture of the system; it confines the field of view of each detector element to 3° (f/18.5) for Module 01 and 4° (f/14) for Module 02. The solenoid-operated cold aluminum shutter placed below the limiting aperture is used to isolate the array from the blackbody radiation when necessary. The temperature of the limiting aperture, as well as that of the cold shutter, can be monitored using the two sensors attached to them. In order to prevent 77-K radiation from leaking from the liquid nitrogen jacket into the detector area, the blackbody, the limiting aperture, and the shutter are all housed inside a baffle box attached to the cold plate.

The detector assembly is housed inside two baffle boxes, both of which are attached to the cold plate. Every precaution is taken to ensure that the baffle boxes are light tight so that the only

radiation on the array is from the blackbody. All baffle boxes are painted black on the inside with Ames 24E infrared-absorbing paint to reduce stray radiation. The wires to the focal-plane electronics are anchored to the cold plate and are connected to the outside through light-tight feedthroughs.

The low-background environment is established using a stack of four cold filters and four cold apertures placed between the filters. The filters and the aperture disks are placed inside a cylindrical holder attached to the cold plate. The combination of the four filters provides a spectral window $1.25\text{ }\mu\text{m}$ wide (full width at half maximum) centered at $106\text{ }\mu\text{m}$. The unwanted radiation over the entire active range of the array outside this bandpass window is either absorbed or scattered. The cold filters used are the following:

1. A free-standing mesh Fabry-Perot bandpass filter. The Fabry-Perot was made in-house by stretching 1000-line/in., free-standing copper mesh (ref. 11) (Buckbee Mears Operation) over a precision-made stainless steel ring. Two such reflectors were then placed in parallel, separated by a precision steel shim-stock spacer about 0.004 in. thick. This Fabry-Perot was designed to have its second order centered at about $100\text{ }\mu\text{m}$ with a finesse of about 50, a bandwidth (full width at half maximum) of about $1.0\text{ }\mu\text{m}$, and a free spectral range of 50 cm^{-1} . Considering the imperfections and losses in the meshes and the error in measuring the thickness of the shim-stock spacer, a deviation from the designed parameters was expected. With the Fabry-Perot cooled to 4.2 K, a high-resolution (0.1 cm^{-1}) spectral transmission test using a Beckman interferometer indicated that the second order of this Fabry-Perot peaks at about $105.9\text{ }\mu\text{m}$ (94.45 cm^{-1}), is about $1.25\text{ }\mu\text{m}$ (1.1 cm^{-1}) wide, and is 50% transmissive. The free spectral range is, therefore, 47.2 cm^{-1} , and the finesse is about 43.

2. A single-crystal KCl Reststrahlen filter. This is a 2-mm-thick disk with 60% transmission at $106\text{ }\mu\text{m}$.

3. A diamond-scatter low-pass filter. This filter was made by depositing $30\text{-}\mu\text{m}$ diamond powder on 0.001-in.-thick white polyethylene. Its measured transmissivity is 85% at $106\text{ }\mu\text{m}$.

4. A black polyethylene low-pass filter. This is a 0.006-in.-thick sheet sandwiched between two copper aperture disks, and it is 70% transmissive at $106\text{ }\mu\text{m}$.

The spectral transmissions of the filters were measured on a Beckman Fourier-transform interferometer at 4.2 K; they are shown in figures 2 through 5. Similar Fabry-Perots were measured using the Bruker interferometer at the Jet Propulsion Laboratory (Pasadena, Calif.) as a cross-check. The results were consistent and repeatable. A combined transmission plot of the filter stack is obtained by multiplying the individual plots (fig. 6).

The cold-limiting apertures placed between the filters define a solid angle rejecting all the radiation outside the cone. The apertures were painted black to absorb any radiation incident on them. The combination of the spectral and spatial filtering not only ensures a low-background environment, but also enables us to determine the exact amount of radiation on the detector.

DETECTOR ARRAY MODULE 01

Detector Assembly

The detector array Module 01 consists of eight discrete front-illuminated detector elements, only four of which are active, placed in a row and indium-soldered to a common bias board. The active detectors, along with their cold electronics, are designated in this report as channels 3 through 6, to be consistent with the Aerojet report (ref. 9). Each detector element is 1×1 mm on the front face and about 2 mm long. The back face of each detector is beveled at 18° to increase the absorption length by inducing total internal reflection (ref. 12). The array is connected to the readout circuitry by pressure contact between the detectors and the indium pads deposited on the sapphire circuit board. Because of the difficulty in using an integrated multiplexing chip, the readout circuitry was made of discrete MOSFETs. Although this is not the optimum configuration for achieving low-noise, background-limited operation, it was implemented to demonstrate the potential of the array for low-background astronomy. The temperature of the array is monitored by a calibrated carbon resistor attached to the back of the circuit board.

Focal-Plane Electronics

The typical circuit for a single unit cell is shown in figure 7. Each cell operates in an integration-reset multiplexing scheme using discrete p-channel M104 MOSFETs for switching and AT4-163 MOSFETs for the output source followers. The integrating element is the node capacitance at the gate of the output MOSFET, which includes all the parasitic capacitances associated with the MOSFET switches, the gate of the output MOSFET, and the connecting leads. The photocurrent generated by the detector is integrated on the node capacitance, and the signal voltage at the end of the integration time is made available through the output source-follower MOSFET.

It was found that the reset switches generate a relatively large current during the reset pulse, which results in a charge-injected voltage of about -500 mV. This unwanted voltage, which is different for each unit cell, is larger than the detector bias and must be compensated for in order for the detector to remain in the proper bias range. Applying $+250$ mV at the bias terminal results in a net bias of about -250 mV across each detector. Since the bias terminal is common to all the detectors, the net bias across each detector is not the same, a result of the nonuniformity in the charge-injected voltage created by the MOSFET switches. Given the present circuit design, it is possible to reduce this dc nonuniformity by setting the reference voltage for each detector element accordingly. Having equal signals at the gates of the source-follower MOSFETs, however, does not guarantee equal output signals; this is because of the different MOSFET thresholds and gains. The output signals can be made equal by adjusting the reference voltages, but only at the expense of making the input signals and, therefore, the net bias voltages, unequal.

Node Capacitance and Gain

In order to evaluate the performance of the array, it is necessary to measure the total capacitance of the unit cell at the gate of the output source follower. This capacitance, which is inherent to the

unit cell, is a combination of all of the parasitic capacitances at this node and is responsible for the charge integration. The gain of the output source follower also needs to be measured; it is used in the calculation of the responsivity of the detector elements.

The gain of each of the output MOSFETs is measured by injecting an ac signal at the V_{ref} node of the desired unit cell, with the reset and the enable MOSFETs of that cell turned on. The signal at the source of the output MOSFET provides the gain. Figure 8 shows the circuit configuration for this measurement.

To measure the node capacitance, a 2.2-pF capacitor is connected to the gate of the channel 3 output MOSFET. Total node capacitance for this channel is the sum of this capacitance and the cell capacitance. Figure 9 shows the circuit configuration for this measurement. By injecting an ac signal at the open end of the external capacitor and measuring the signal at the source of the channel 3 output MOSFET, one can calculate the total capacitance of this channel using the following formula:

$$C_t = (g_0/g_c) C_e$$

where g_0 is the source-follower gain with the signal injected at V_{ref} , g_c is the gain with the signal injected at the external capacitor node, and C_e is the external capacitance (in this case, 2.2 pF).

External capacitors are not provided for the other channels. It is assumed that the capacitances of all the cells are identical so that the measurement of the total capacitance of channel 3 can be used to calculate the node capacitances of the other channels. The result of the gain and node-capacitance measurements are given in table 1.

Responsivity and Dark Current

The response of the Module 01 detector array could only be measured under static operation, which involves the direct measurement of the photocurrent of each individual detector in a nonmultiplexed mode. The array could not be multiplexed because of the high leakage current which was attributed to faulty MOSFET switches and/or a malfunctioning electronics board.

For the static measurements, the reset and the enable switches of the detector under test were turned on, and all the other channels were turned off. None of the output source-followers were powered. The photocurrent of the detector was then measured directly by an electrometer (Keithley 642) connected to the V_{ref} node. A typical unit-cell circuit for static measurements is shown in figure 10.

As the first step, the dark current-voltage (I-V) characteristic of channel 3 was measured at different ambient temperatures. The dark background is established when the blackbody and all the other components in the optical path are at the He-bath temperature, in which case the detector's field of view is 180°. The dark I-V measurement, in addition to giving us the detector's dark current, would reveal the detector's breakdown voltage and, therefore, the optimum (or near-optimum) operating point. The results of this test are shown in figure 11. The breakdown occurs at about ± 300 mV, which is lower than expected. The low breakdown voltage may occur because the detectors are made of low-compensation material, or it could be due to poor contact electrodes. The dark

currents of the other channels were determined with the array biased at -264 mV, which is thought to be nearly an optimum operating point just below the breakdown voltage.

The results of these tests indicate that channels 3 and 4 have similar dark currents which are lower than those of the other two channels. Channels 5 and 6 were excessively noisy at 4.2 K, but much quieter at lower temperatures. The dark current of the array at 3.0 K is about three orders of magnitude lower than that at 4.2 K. This suggests that the individual detectors in the array may exhibit a lower noise equivalent power (NEP) at 3.0 K. The NEP of the system, however, may be limited by the switching noise, defeating the detector's noise advantage. It should be noted that the leakage current of the MOSFET switches, which is small but nonzero, and any other spurious current were compensated for by subtracting out the zero-bias offset current. No effort was made to measure the leakage current of the MOSFET switches. Table 2 summarizes the results.

In order to determine the responsivity of the detectors, it is necessary to calculate the total amount of the background flux. Since the filter stack limits the radiation seen by the detectors to a very narrow spectral window, the blackbody radiation as well as the detectors' responsivity can be considered constant over the effective bandwidth of the filter. The total flux, then, is the radiation flux density at the center of the filter, within the detectors' solid angle, multiplied by the bandwidth of the filter.

The responsivities of channels 3 and 4 were measured by measuring each detector's photocurrent as a function of the incident power. The detectors were biased at -264 mV. The blackbody temperature was varied from 5 K to 75 K, providing the radiation power ranging from 9.85×10^{-21} W (5 photons/sec), corresponding to dark background, to 8.94×10^{-13} W (4.8×10^8 photons/sec). In this power range, the responsivity should be independent of the incident radiation if the system performs as designed and the detectors only see the in-band radiation from the blackbody. In fact, the photocurrent-versus-incident-power test was done to check the integrity of the system. The responsivities of channels 5 and 6 were measured at a single incident power level. The tests were carried out at 4.2 K and 3.0 K.

The results of the experiment, shown in figure 12 for channel 3, indicate a linear relationship between the photocurrent and the incident power, as expected. The slopes of the lines are the responsivities of the detector at the designated operating temperature. The responsivities of the detectors were lower at temperatures below 4.2 K. This was not expected, for previous tests on other Ge:Ga detectors done by the authors as well as other investigators had indicated a peak response at about 3.0 K (ref. 5). The reason for this anomaly was not investigated. A summary of the measured responsivities is given in table 2.

Further tests were carried out on channel 3 to determine its response as a function of the bias voltage. For these tests the array was at 4.2 K and the blackbody temperature was kept at 40.0 ± 0.1 K, corresponding to an incident power of 1.59×10^{-13} W (8.5×10^7 photons/sec). The results are plotted in figure 13.

Noise Measurements

Considering that Module 01 could only be run in the static mode, and that modified circuitry (such as a transimpedance amplifier with a cold front end) was required to run the tests, the noise performance of this module was not determined. In addition, such a test would be of little value since it would not reflect the read noise of the system, which is expected to be the dominant source of noise and is the main objective of our investigation here.

DETECTOR ARRAY MODULE 02

Detector Assembly

The detector array Module 02 consists of eight discrete detector elements, only two of which are active. The detector geometry is identical to that of Module 01. Unlike Module 01, however, this array has two discrete unit cells each having integrated MOSFETs. The semimonolithic design should provide better performance than the discrete MOSFET design of Module 01. To be consistent with Aerojet's report (ref. 9), we refer to these detectors along with their cold electronics as channels 5 and 6. The temperature of the array is monitored by a calibrated carbon resistor attached to the back of the circuit board.

Focal Plane Electronics

The typical circuit for a single unit-cell is shown in figure 14. Each cell operates in an integration-reset multiplexing scheme identical to that of Module 01. Module 02 provides the capability for injecting a signal at the detector node ($V_{\text{reset-not}}$) to compensate for the charge-injected signal generated during the reset pulse.

Node Capacitance and Gain

The gain of the output source follower and the node capacitance of each unit cell were measured following the procedure described previously, using the circuit configurations shown in figures 8 and 9. The external 2.2-pF capacitor is connected to the gate of channel 5. The output MOSFET of channel 6 was damaged, so channel 6 was completely inoperative. Channel 5 had a source-follower gain of 0.84 and a node capacitance of 4.7 pF.

Responsivity and Dark Current

The response of the array was determined in two ways: statically, which involves the direct measurement of the photocurrent of each individual detector in a nonmultiplexed mode; and dynamically, which involves measurement of the charge-integrated signals at the output of the source followers under multiplexed operation.

Static measurements—Following the procedure described earlier, several tests were conducted on the Module 02 array to determine its responsivity and dark current under static conditions. Only

channel 5 was tested, because there were problems with the focal-plane electronics of the other channel. Figure 15 shows the dark I-V of this detector. This array shows a higher breakdown voltage than Module 01, perhaps because of better contact electrodes. The detector's dark current at temperatures below 4.2 K, however, is very poor compared with that of Module 01. Surface contamination of the detector, among other possibilities, could be a contributing factor.

With the array at 4.2 K, the photocurrent of channel 5 was measured as a function of the incident power which ranged from 9.85×10^{-21} W (5 photons/sec) to 1.56×10^{-12} W (8.3×10^8 photons/sec). The detector was biased at -264 mV to provide a direct comparison with Module 01 measurements. The more appropriate operating point for this detector, however, is about 350 mV. The response of the detector was also measured at temperatures below 4.2 K, which again showed an unexpected drop at lower temperatures. The results are plotted in figure 16 and are summarized in table 3. A plot of the responsivity versus the bias voltage is shown in figure 17. For this test, the blackbody temperature was controlled at 40 K, corresponding to an incident power of 2.77×10^{-13} W (1.5×10^8 photons/sec). Overall, this array showed higher responsivity than Module 01.

Dynamic measurements— Since only channel 5 of this array was operative, the dynamic tests on Module 02 could only be carried out by either turning the channel on and off, which is referred to as continuous operation, or multiplexing it with the “pseudochannel” that was provided with the array. Neither of these schemes is optimum for characterizing the array; however, the tests would provide some useful information.

In the continuous-operation mode, the V_{ref} node is grounded and the reset switch is clocked at a particular frequency; 500 Hz was chosen as the nominal sampling (clocking) frequency. In this mode, the source-follower MOSFET is continuously powered and the clock period controls the integration time. The signal at the source-follower output is buffered through a preamp and is directly monitored on an oscilloscope. The sample-and-hold circuitry is bypassed. Figure 18 shows the circuit configuration.

The detector photocurrent charges up the node capacitor until the reset switch is closed and the detector node is clamped to V_{ref} , which is grounded in this case. If the integration time is long enough (low sampling frequency), the increasing signal at the node will debias the detector and the signal will reach an asymptotic value. Therefore, a detector with a high breakdown voltage not only offers higher responsivity but provides better dynamic range. Figure 19 shows the output signal as a function of time for different incident power levels. For all these measurements, the detector bias was +350 mV, its temperature was 4.2 K, and the total integration time was 2 msec, corresponding to a 500-Hz sampling rate. The debiasing of the detector is apparent in these plots. Using the output voltage, the gain, and the node capacitance values measured earlier, the responsivity of the detector can be calculated. The result is in agreement with the static measurements. The signal was also measured at the output of the sample-and-hold, which gave the proper dc signal consistent with the analog signal measured directly at the source-follower's output.

Noise Measurements

Module 02 noise tests were conducted with the array running in the continuous mode. The detector temperature was 4.2 K and the blackbody temperature was raised from ambient (for dark tests) to 75 K (1.56×10^{-12} W, 8.3×10^8 photons/sec). A fast Fourier transform spectrum analyzer (Hewlett Packard 3561A) was connected to the output of the sample-and-hold (fig. 18). The gain of the preamp was set to 10. The noise spectrum of the system was obtained at different sampling frequencies, as shown in figure 20. The spectrum is relatively flat at frequencies below the sampling rate. The dominant 60-Hz noise spike and its harmonics posed a problem, but they could be reduced to acceptable levels by proper grounding and shielding of the wires. The presence of the 60 Hz and its harmonics is even more pronounced, for they generate a broadband noise spectrum by beating against the sampling frequency. No significant change in the noise level was seen as the blackbody temperature was increased, which suggests that the array was not background-limited, at least not up to the 1.56×10^{-12} W background levels. The low dynamic range of the detector and the high MOSFET noise are the main reasons for not achieving (low) background-limited performance. The sample-and-hold noise spectrum at different frequencies was also measured by shorting its input. These results are also given in figure 20.

Figure 21 is a plot of the dark-system noise density (at the sample-and-hold output) and the sample-and-hold noise density (sample and hold shorted) as a function of sampling frequency using the flat parts of the spectra similar to the spectra presented in figure 20.

Considering that the preamp gain is 10, the sample-and-hold seems to be the dominant source of noise at higher sampling frequencies, whereas the source-follower MOSFET noise becomes dominant at lower frequencies. For background-limited performance, the array should be run with the highest possible system gain to overcome the sample-and-hold noise. The MOSFET noise, on the other hand, must be dealt with at the fundamental stage of the design.

The total rms noise, V_n , at the sample-and-hold output, is the integral of the noise-density spectrum of figure 20. It can be approximated, using the following relationship, by assuming that the noise density is constant (a reasonable assumption at frequencies well below the sampling frequency) and that the samples are uncorrelated:

$$V_n = v_n (f_s/2)^{1/2}$$

where v_n is the noise density and f_s is the sampling frequency.

A more useful representation of the system noise would be the read noise (electrons/sample) referenced back to the output of the detector. The read noise can be calculated by using the rms noise, the integration capacitance, and the total system gain, as follows:

$$n = (C_t V_n)/g_t e$$

where C_t is the total integrating capacitance; g_t is the system gain, source-follower and preamp; and e is the electronic charge.

Figure 22 is a plot of the dark-system read noise as a function of sampling frequency. The solid curve is the best fit to the data points. The large deviation of the fit from 10 to 100 Hz is due to the dominant 60-Hz noise and its harmonics.

The NEP of the system, referenced back to the detector, is calculated using the following relationship:

$$\text{NEP} = i_n/R, \text{ with } i_n = v_n C_t f_s/g_t$$

where i_n is the current noise density referenced to the detector, and R is the current responsivity.

It should be noted that because of the limited dynamic range of the detector, the responsivity depends on the sampling frequency; therefore, it should be modified to account for the debiasing of the detector at low frequencies. The proper scaling factor was obtained by measuring the signal as a function of the sampling frequency and finding a frequency (10 kHz in this case) beyond which the signal saturation was negligible.

Using the above relationship and the scaling factor for the responsivity, the NEP of the system as a function of sampling frequency was determined. Figure 23 is a plot of the results. The solid curve is the best fit to the data points.

It is apparent from the NEP plot that the optimum sampling frequency is between 200 Hz and 2 kHz. At lower sampling rates the detector is debiased and the output signal is saturated. MOSFET noise of the multiplexing cell, which typically has a $1/f$ component, becomes dominant and degrades the overall signal-to-noise ratio of the system. At higher sampling rates, although the electronics noise drops, there is not enough time for the signal to build up, and again the signal-to-noise ratio suffers. It should be noted, however, that the optimum sampling frequency is background dependent and would be higher for higher background levels.

It is conceivable that the array would exhibit better noise performance at temperatures below 4.2 K. This is particularly true for the individual detector elements, since at 3.0 K, the dark current drops by a factor of about 7, whereas the responsivity is reduced only by about 25%. However, since the system is MOSFET-noise dominated, the full effect of the detector noise advantage at 3.0 K may not be realized. Noise tests at temperatures below 4.2 K required additional electrical shielding, and were postponed.

CONCLUDING REMARKS

We have studied the performance of two multielement Ge:Ga detector arrays under static and multiplexed operation in the far infrared. Both arrays and their support electronics were developed at Aerojet ElectroSystems and were tested prior to delivery to Ames Research Center. The purpose of our study was twofold: (1) to determine the fundamental parameters of the arrays under multiplexed operation and to evaluate their applicability to low-background astronomy, and (2) to cross-check the results reported by the Aerojet team and to clarify some of their anomalous results.

Both arrays, referred to as Modules 01 and 02, consist of eight discrete Ge:Ga detector elements placed side by side in a linear arrangement. Because of the problems with the focal-plane circuitry, however, not all eight elements in each array were active. Module 01 was delivered as a 1×4 - (active) element detector array with discrete MOSFETs and Module 02 as a 1×2 -element array with two discrete unit cells but integrated MOSFETs for each cell. Module 02 is considered to be a better design, since, because of its semimonolithic focal-plane electronics, it is theoretically capable of superior noise performance.

Module 01 was equipped with a stressing mechanism that, if used, would have extended the spectral range of the array to longer wavelengths. Because of design problems, however, the mechanism could not be used, and the module was delivered to Ames unstressed.

As the first step and in order to ensure the integrity of each detector element, a number of tests were conducted on these arrays under static operation. The responsivity of each detector was measured at different temperatures and bias levels. Only Module 02 could be tested in dynamic mode. The results are summarized below.

1. Two (out of four) channels of Module 01 were excessively noisy, so a limited number of measurements were taken on these channels. Module 02 had only one operating channel; the second channel had faulty MOSFETs.

2. Because of a very high leakage current, Module 01 could not be tested in the multiplexed mode. In addition, since only one channel of Module 02 was operative, the dynamic tests on Module 02 could only be carried out by either turning the channel on and off or multiplexing it with a "pseudochannel," neither of which is a realistic mode of operation.

3. At 4.2 K and with the detectors biased at -264 mV, the responsivity was measured and found to be about 300 A/W, which is higher than expected. This may be because of the detector's beveled end which could substantially improve the quantum efficiency by inducing total internal reflection. Assuming unity quantum efficiency, photoconductive gain would be 3.5, which is high but not unreasonable. Our responsivity calculations rely on a cryogenically cooled filter stack which precisely defines a narrow spectral window at $106 \mu\text{m}$ with a definite radiation solid angle. The results are consistent with the Aerojet results, which are based on measuring the average responsivity of the array over the entire active range of the detector and subsequently using that average to *calculate* the responsivity at $100 \mu\text{m}$.

4. The responsivity of the individual detectors, even within the same module, was only uniform to within 25%. Considering that all detector elements in both arrays were constructed from the same wafer, it is speculated that some have better and more uniform contact electrodes and thus provide a more efficient active region along the length of each detector.

5. The breakdown voltage of both arrays was about ± 300 mV, which is lower than expected; Module 02 had higher breakdown voltage than Module 01. This could be because of the low-compensation detector material or poor contact electrodes, or both. Better procedures for making the contact electrodes could result in a higher breakdown voltage, which would both increase the responsivity and improve the dynamic range of the array.

6. The dark current of both modules showed significant improvement as they were cooled below 4.2 K. Module 01, however, was substantially better in this regard than Module 02.

7. The responsivity of both arrays dropped as they were cooled below 4.2 K. Aerojet tests indicated similar results. From the previous work on Ge:Ga detectors, the maximum response of the detector was expected to be at about 3 K.

8. The gain and node-capacitance measurements yielded satisfactory results consistent with Aerojet's reported values.

9. In the dynamic mode, the responsivity of the single channel of Module 02 agreed with the results from the static measurements. Detector debiasing, however, is a point of concern. At a 500-Hz sampling rate, the array was clearly in saturation because of the low bias voltage.

10. Both the sample-and-hold and the multiplexed signal showed a $1/f$ (sampling frequency) dependence. The sample-and-hold noise can easily be overcome by increasing the system gain. The MOSFET noise, however, is a more serious problem and will have to be dealt with at the design level.

11. At 4.2 K and with the detector biased at 350 mV, the optimum system read noise was 6100 electrons/sample and the NEP was $1.0 \times 10^{-16} \text{ W}/\sqrt{\text{Hz}}$. The low (up to $1.56 \times 10^{-12} \text{ W}$, 8.3×10^8 photons/sec) background-limited performance was not achieved, primarily because of the limited dynamic range and the high MOSFET noise. Although noise tests at temperatures below 4.2 K were not carried out, it is conceivable that the array would exhibit better noise performance at about 3.0 K.

The effort reported herein should be recognized as a starting point for future developments of integrated far-infrared detector arrays for low-background astronomy. Considering that certain aspects of the system fell short of the optimum design configuration generally seen in state-of-the-art systems, the results were informative and, at least for some parts, encouraging. The lack of more conclusive results can be attributed primarily to the fact that the arrays were not perfected to the point that reliable data could be obtained. Even at the discrete detector level, the arrays did not perform as well as they should have. The large difference in the responsivity of the detector elements and the low breakdown voltage would degrade the overall performance of the array. The nonuniformity of the output MOSFETs is a serious problem which is magnified by the low breakdown voltage of the detectors. It is conceivable that even with the detectors at their peak performance, this nonuniformity would impose severe limitations, in which case a different type of MOSFET with more uniform characteristics may be a logical approach. The charge injection generated by the MOSFET switches during the reset pulse is clearly another drawback, especially considering that it is larger than the detector bias. Compensating for this transient signal is not a viable solution, for the detector becomes unstable and noisy when it crosses the zero bias point.

It is clear that the multiplexing scheme and the integrated circuit technology used with shorter wavelength detectors with very large breakdown voltages are not applicable to Ge:Ga photoconductors. The low breakdown voltage of Ge:Ga poses some fundamental problems that require close attention at the early stages of focal-plane circuit design. The situation is further complicated if one

wishes to extend the long wavelength response of the detector array by applying uniaxial stress. Use of other far-infrared detectors such as Ge:Ga blocked-impurity-band (BIB) photoconductors, which have inherently larger breakdown voltages and longer wavelength responses, would somewhat alleviate these problems. In either case, however, the development of low-noise cryogenic field-effect transistors appropriate for use with detectors with low breakdown voltage should be considered a crucial part of the overall effort of far-infrared detector array technology.

REFERENCES

1. McKelvey, M. E.; McCreight, C. R.; et al.: Characterization of Direct Readout Si:Sb and Si:Ga Infrared Detector Arrays for Space-Based Astronomy. Proc. SPIE, vol. 868, 1987, p. 73.
2. Werner, M. W.; Murphy, J. P.; Witteborn, F. C.; and Wiltsee, C. B.: The SIRTf Mission, Space Infrared Telescope Facility. Proc. Soc. Photo-Opt. Instrum. Engr., vol. 589, 1986, p. 210.
3. Swanson, P. N.; Breckinridge, J. B.; Diner, A.; and Freeland, R. E.: System Concept for a Moderate Cost Large Deployable Reflector (LDR). Opt. Engr., vol. 25, 1986, p. 1045.
4. Kazanskii, A. G.; Richards, P. L.; and Haller, E. E.: Far Infrared Photoconductivity of Uniaxially Stressed Germanium. Appl. Phys. Lett., vol. 31, 1977, p. 496.
5. Haller, E. E.; Hueschen, M. R.; and Richards, P. L.: Ge:Ga Photoconductors in Low Infrared Backgrounds. Appl. Phys. Lett., vol. 34, 1979, p. 495.
6. Hadek, V.; Farhoomand, J.; et al.: Extension of Long Wavelength Response by Modulation Doping in Extrinsic Germanium Infrared Detectors. Appl. Phys. Lett., vol. 46, 1985, p. 403.
7. Watson, D. M.; and Huffman, J. E.: Germanium Blocked-Impurity-Band Far-Infrared Detectors. Appl. Phys. Lett., vol. 52, 1989, p. 1602.
8. Gornick, E.: Far Infrared Light Emitters and Detectors. Physica, vol. 127B, 1984, p. 95.
9. Development of a Unit Cell for a Ge:Ga Array. NASA CR-177-445, 1988.
10. Smith, S. M.: The Reflectance of Ames 24E, Infrablack, and Martin Black. Proc. SPIE, vol. 967, 1988, p. 248.
11. Pickett, H. M.; Farhoomand, J.; and Chiou, A. E.: Performance of Metal Meshes as a Function of Incidence Angle. Appl. Opt., vol. 23, 1984, p. 4228.
12. Wang, J. Q.; Richards, P. L.; et al.: Optical Efficiency of Far Infrared Photoconductors. Appl. Opt., vol. 25, 1986, p. 4127.

Table 1. Gains and node capacitances of Module 01 unit cells

Channels	Gain	Capacitance, pF
3	0.84	5.78
4	0.88	3.58 ^a
5	0.76	3.58 ^a
6	0.85	3.58 ^a

^aCalculated from channel 3 capacitance.

Table 2. Responsivity and dark current of Module 01 at 4.2 and 3.0 K: Static tests^a

Channels	Dark Current, A ^b		Responsivity, A/W	
	4.2 K	3.0 K	4.2 K	3.0 K
3	-7.5×10^{-11}	-5×10^{-14}	290 ± 42	146 ± 16
4	-7.3×10^{-11}	-5×10^{-14}	309 ± 27	157 ± 19
5	-1.9×10^{-10}	-6×10^{-14}	377	182
6	-1.1×10^{-10}	-1×10^{-13}	334	173

^aBias = -264 mV.

^bNegative currents signify negative bias.

Table 3. Responsivity and dark current of channel 5 of Module 02: Static tests

Bias (mV)	Dark Current, A ^a			Responsivity, A/W		
	4.2 K	3.0 K	2.6 K	4.2 K	3.0 K	2.6 K
-264	-7.1×10^{-11}	-1.1×10^{-11}	-9.4×10^{-12}	337 ± 19	204 ± 18	172 ± 13
+350	$+1.8 \times 10^{-10}$	$+2.5 \times 10^{-11}$	$+2.1 \times 10^{-11}$	584	436 ± 27	380 ± 15

^aNegative currents signify negative bias.

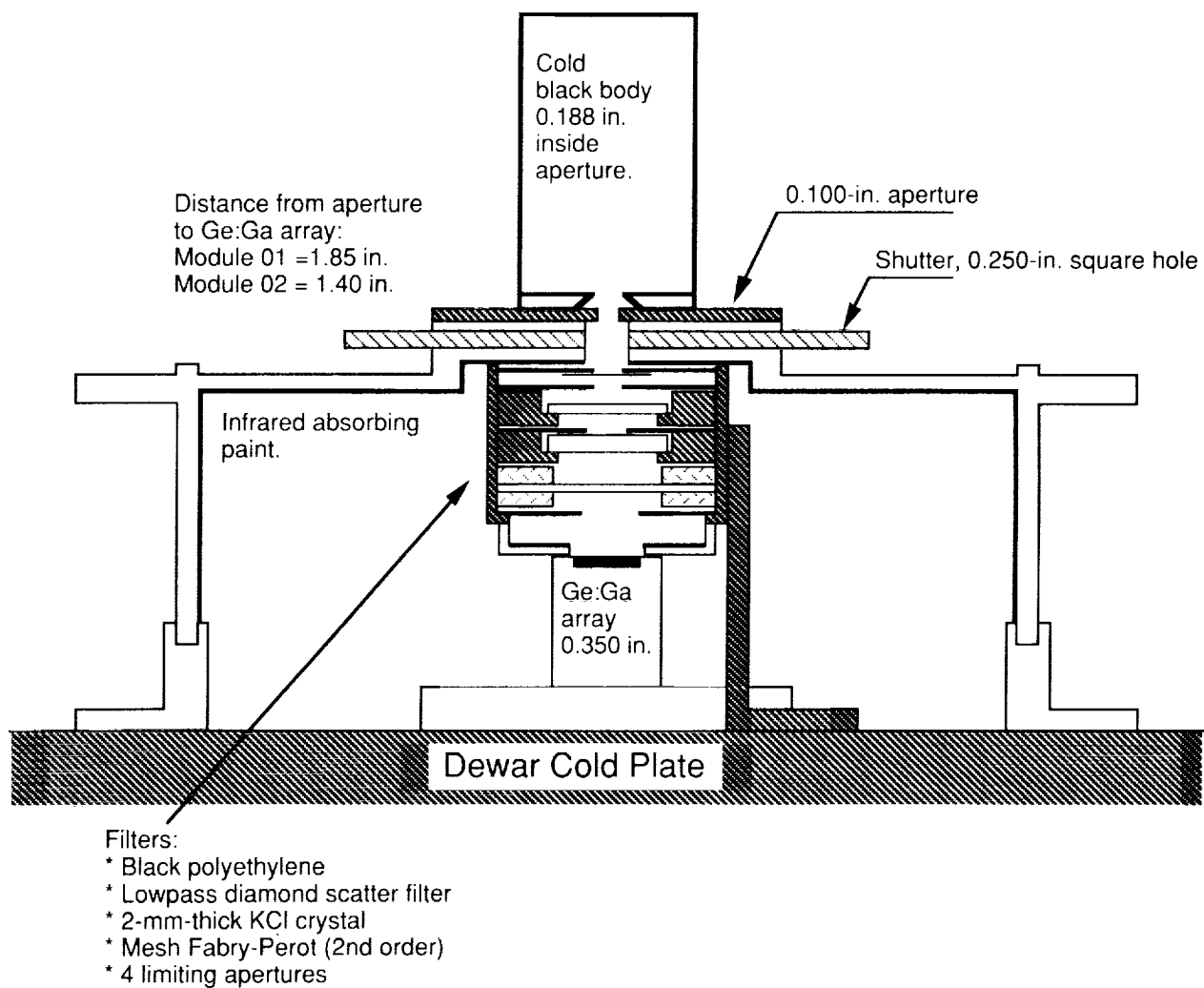


Figure 1. Optical configuration of the detector system.

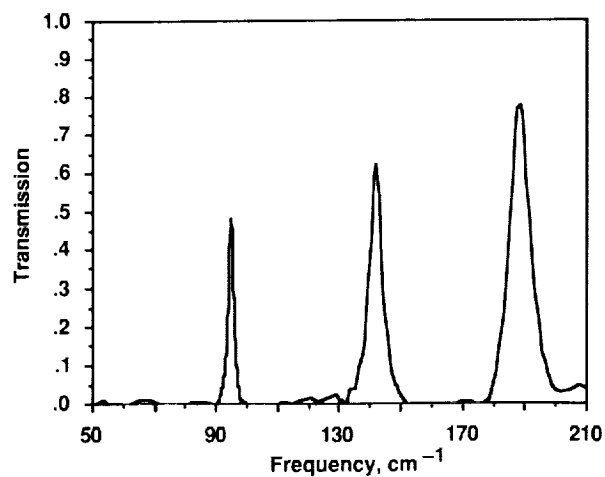


Figure 2. Transmission properties of the copper-mesh Fabry-Perot in the spectral range of the Ge:Ga detector at 4.2 K.

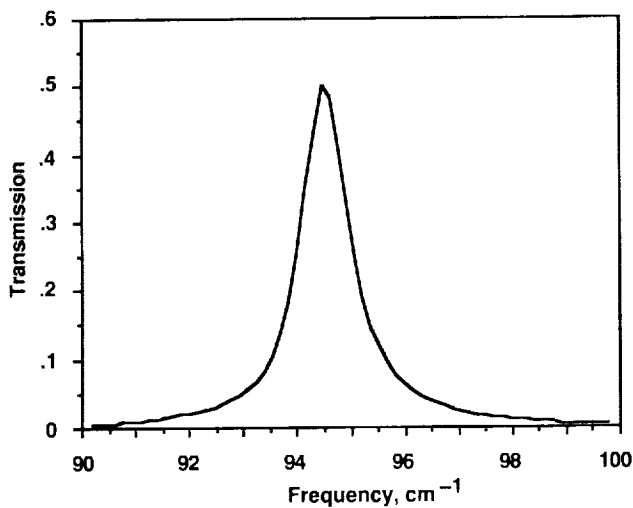


Figure 3. Second order of the copper-mesh Fabry-Perot at 4.2 K.

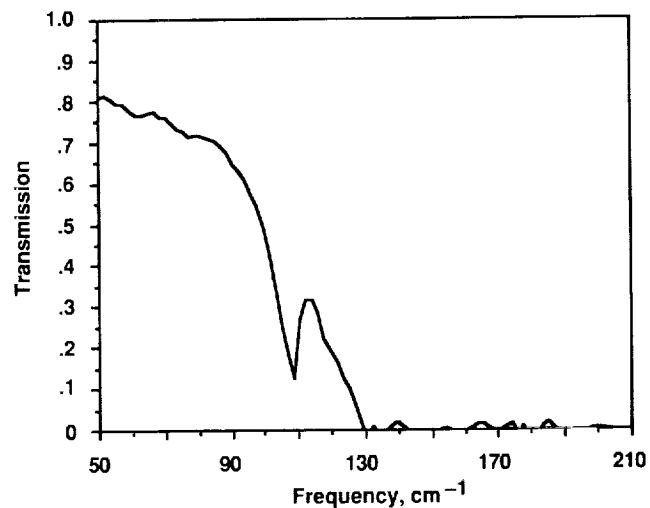


Figure 4. Transmission properties of the 2-mm-thick KCl single crystal in the spectral range of the Ge:Ga detector at 4.2 K.

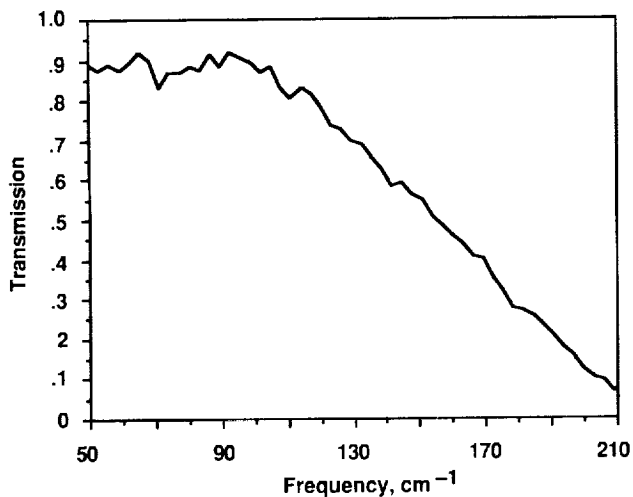


Figure 5. Transmission properties of the diamond scatter filter in the spectral range of the Ge:Ga detector at 4.2 K.

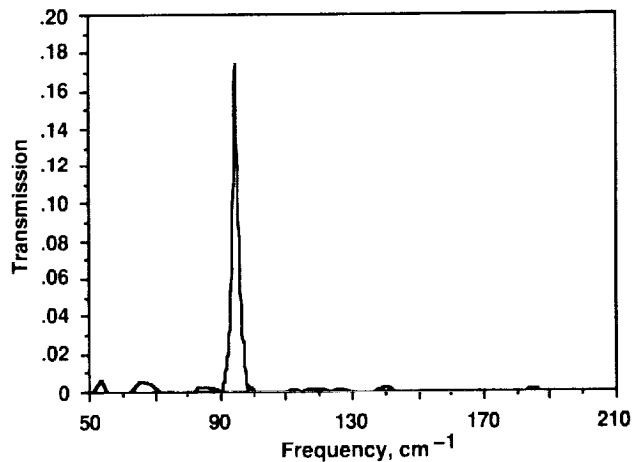


Figure 6. Transmission properties of the filter stack at 4.2 K.

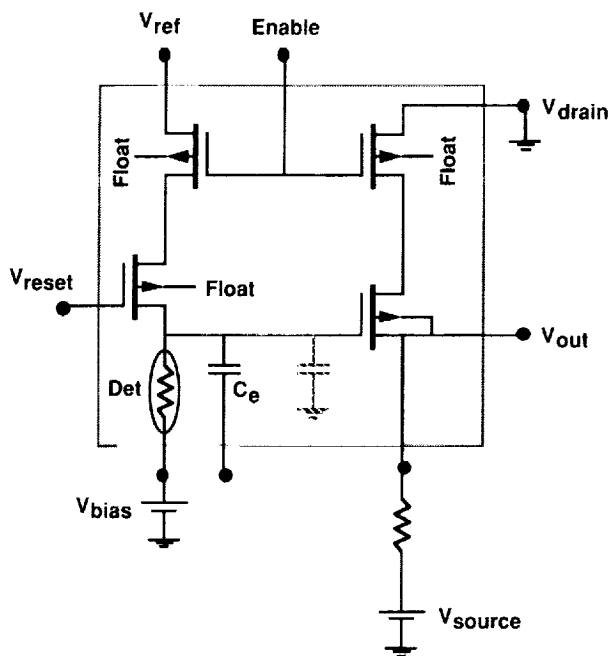


Figure 7. Module 01 multiplexing unit cell. Components in the box are at the focal plane; the capacitor in dashed lines is the cell capacitor; C_e is the external capacitor provided on channel 3 only.

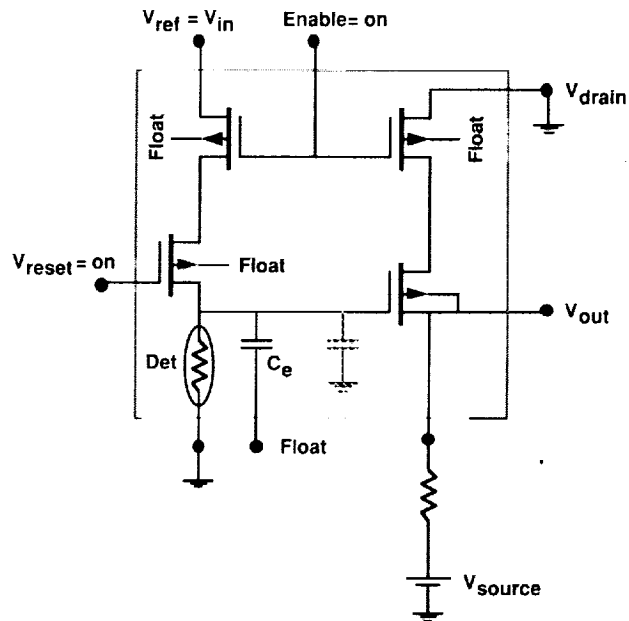


Figure 8. Circuit configuration for measuring source-follower gains.

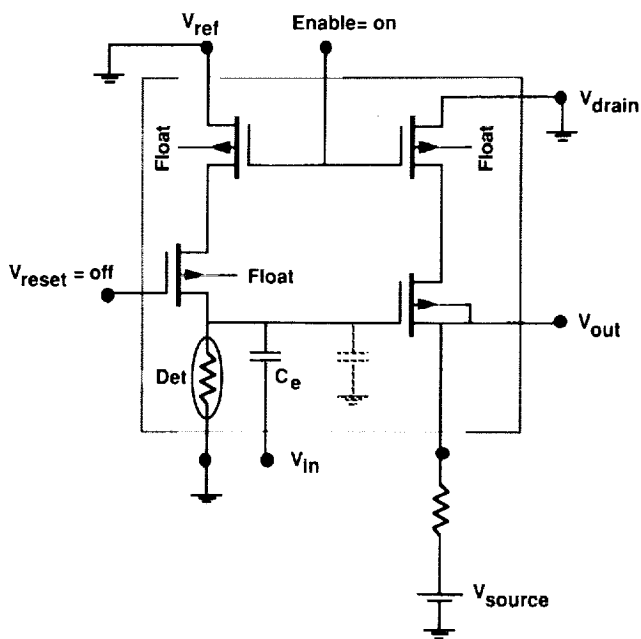


Figure 9. Circuit configuration for measuring node capacitances.

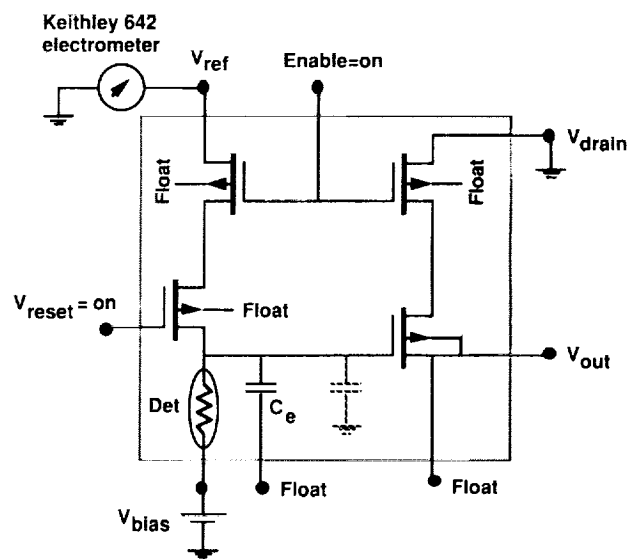


Figure 10. Circuit configuration for static measurement of photocurrent.

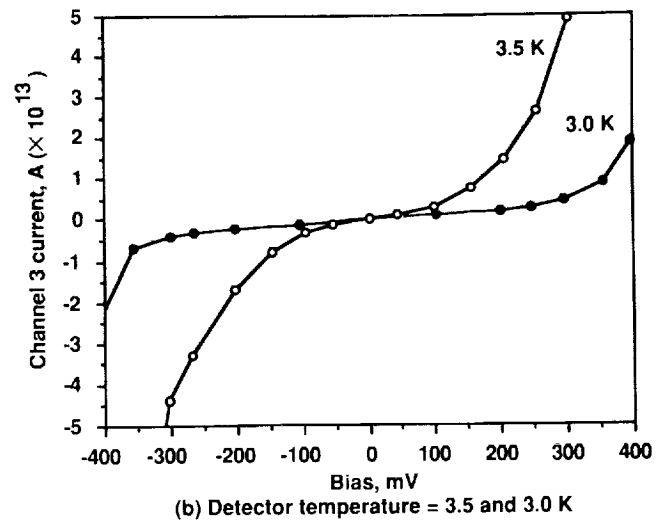
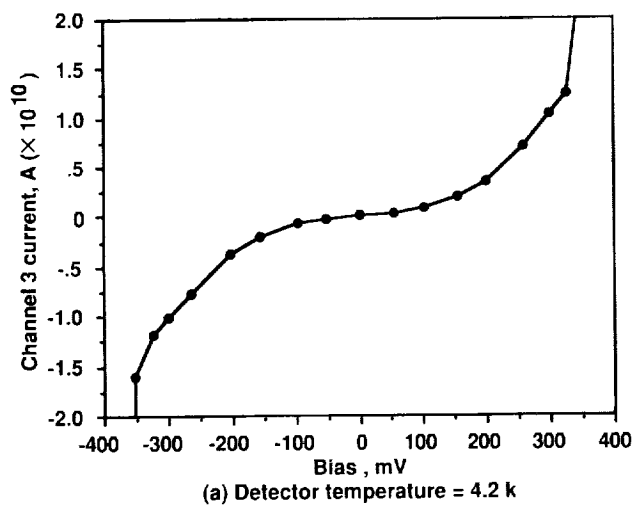


Figure 11. Dark I-V of channel 3 at 4.2, 3.5, and 3.0 K.

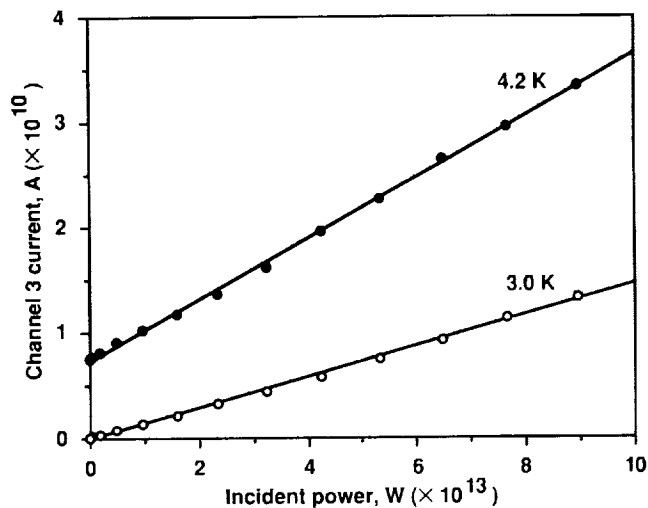


Figure 12. Photocurrent of channel 3 as a function of incident power at 4.2 and 3.0 K. Slopes of lines are responsivities of the detector.

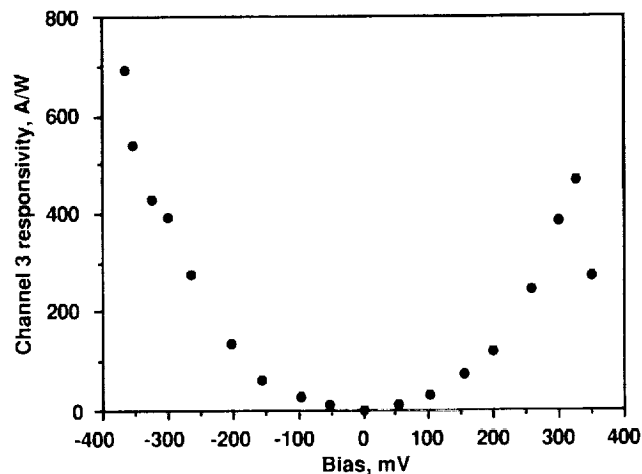


Figure 13. Responsivity of channel 3 as a function of bias. Detector temperature = 4.2 K; background radiation = 1.59×10^{-13} W (8.5×10^7 photons/sec).

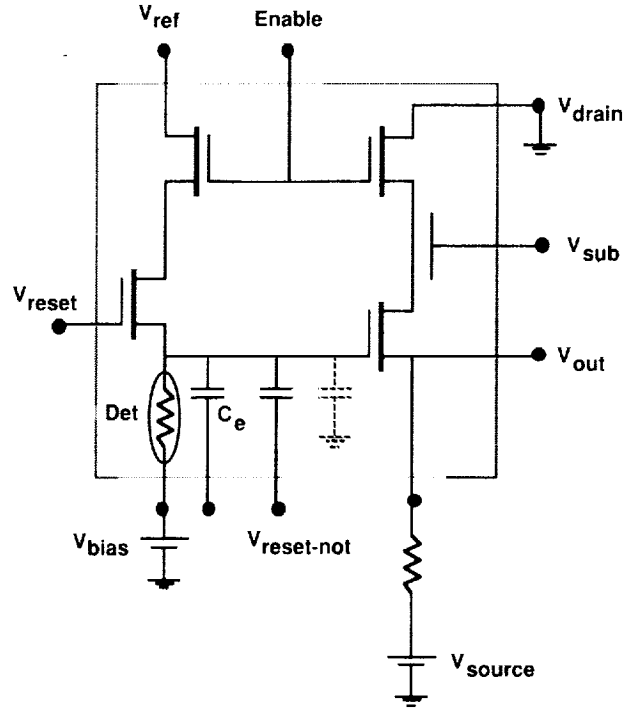


Figure 14. Module 02 multiplexing unit cell. Components in the box are at the focal plane. Signal injected at $V_{\text{reset-not}}$ could cancel out the spurious signal generated during the reset pulse. The capacitor in dashed lines is the cell capacitor; C_e is the external capacitor provided on channel 5 only.

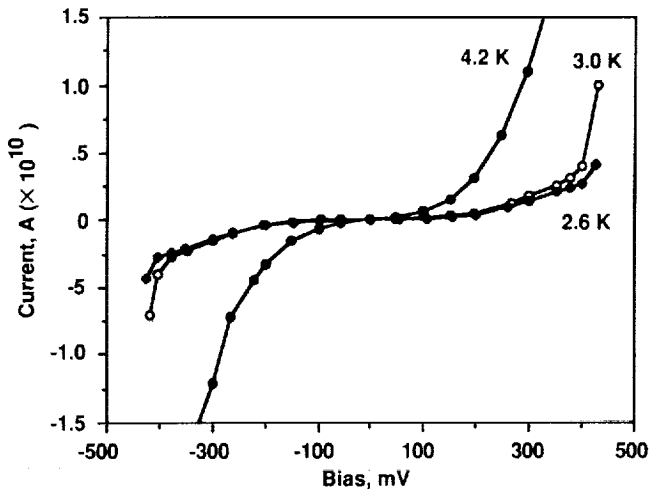


Figure 15. Dark I-V of channel 5.

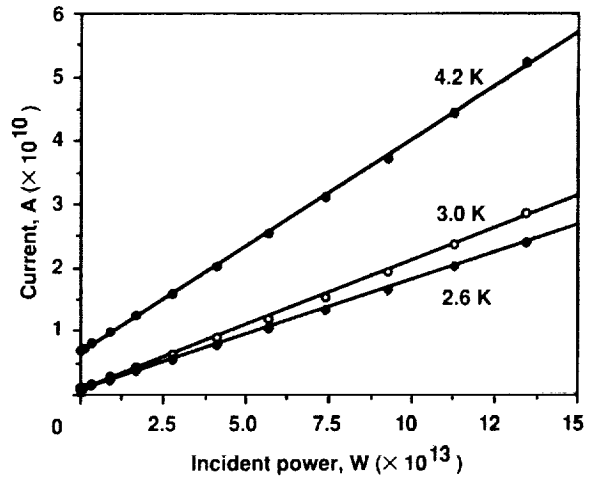


Figure 16. Photocurrent of channel 5 as a function of incident power. Detector bias = -264 mV. The slopes of the lines are the responsivities of the detector.

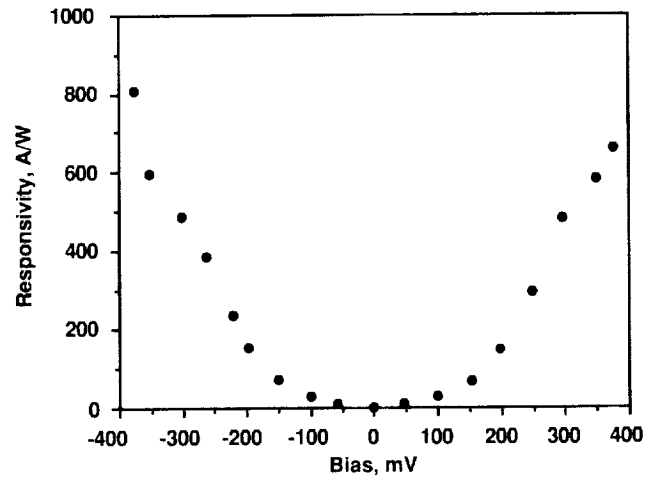


Figure 17. Responsivity of channel 5 as a function of bias. Detector temperature = 4.2 K; background radiation = 2.77×10^{-13} W (1.5×10^8 photons/sec).

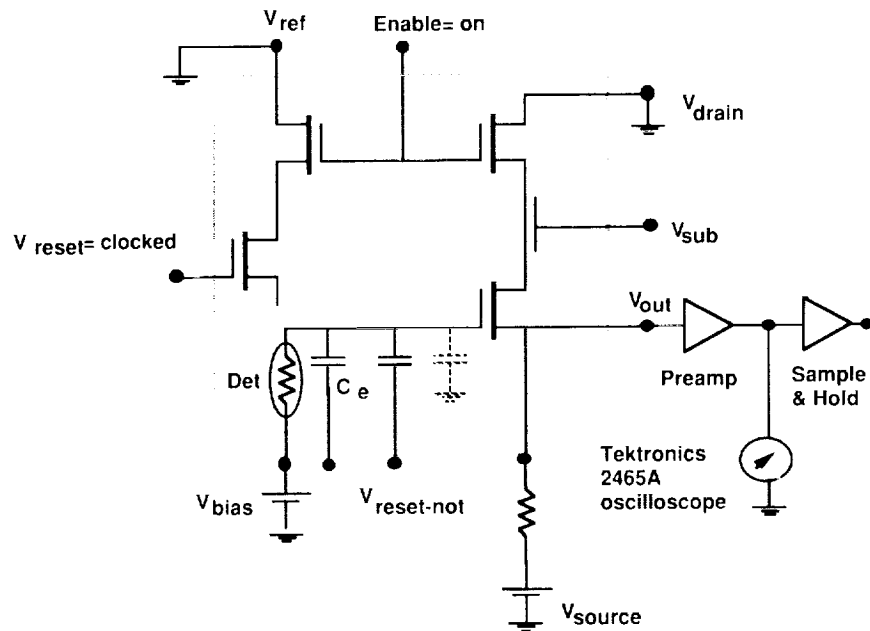


Figure 18. Circuit configuration for dynamic measurement of photocurrent.

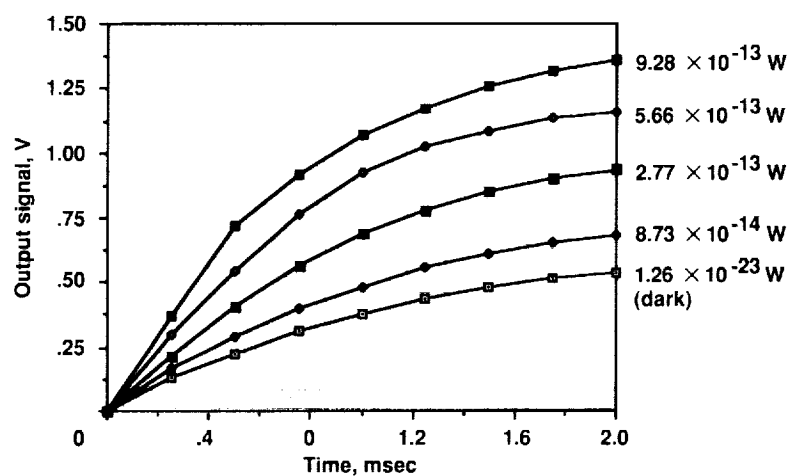


Figure 19. Source-follower output signal as a function of time at several incident power levels. Detector temperature = 4.2 K; bias = 350 mV; total integration time = 2 msec; preamp gain = 10; source-follower gain = 0.84. Signal repeats periodically.

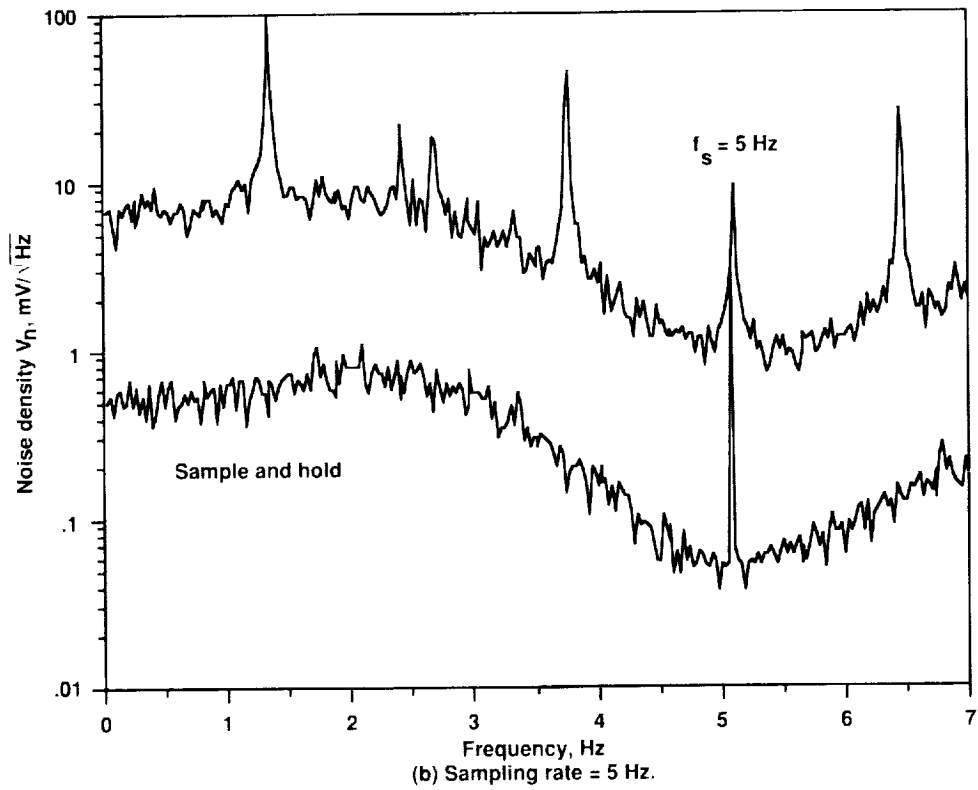
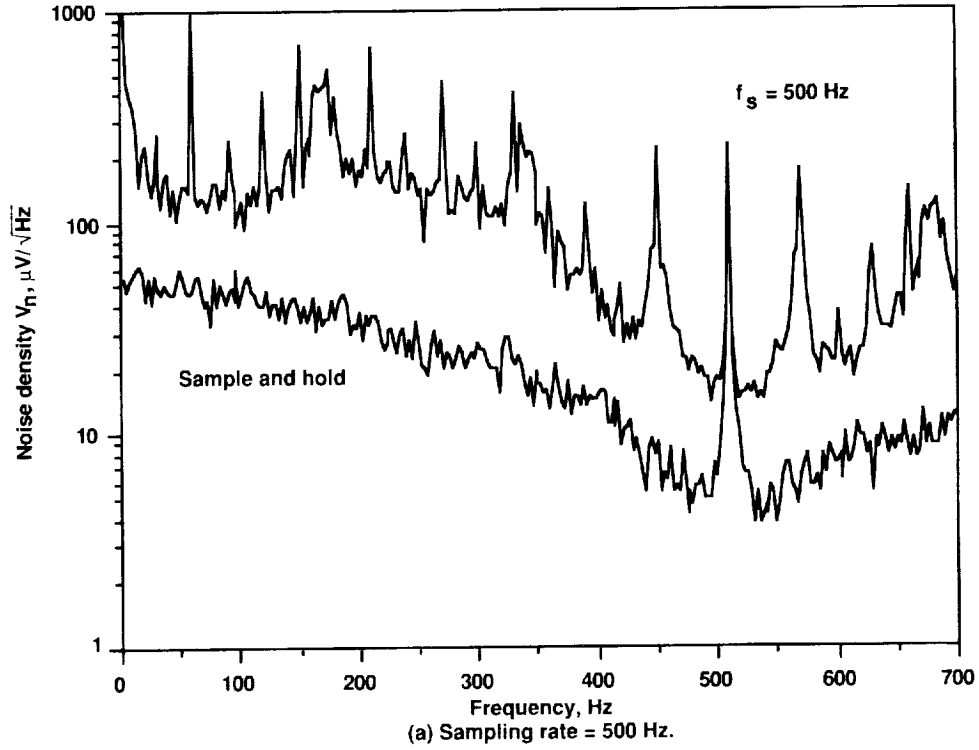


Figure 20. Dark system noise spectrum of Module 02 at 5 and 500 Hz sampling frequencies. Detector temperature = 4.2 K; bias = 350 mV; preamp gain = 10; source-follower gain = 0.84.

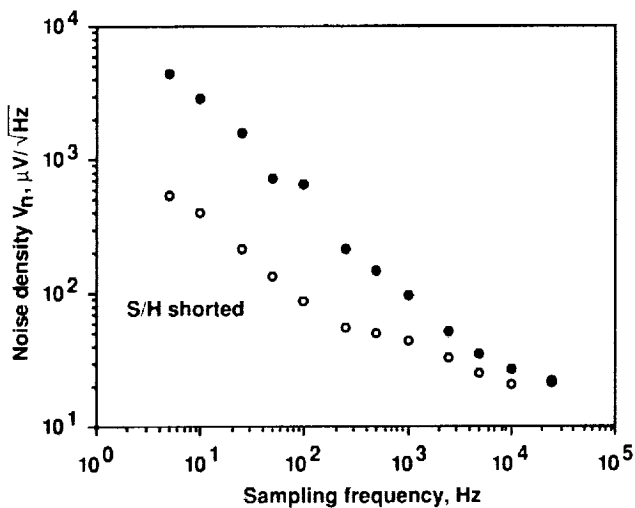


Figure 21. Dark noise density of Module 02 as a function of sampling frequency. Detector temperature = 4.2 K; bias = 350 mV; preamp gain = 10; source-follower gain = 0.84.

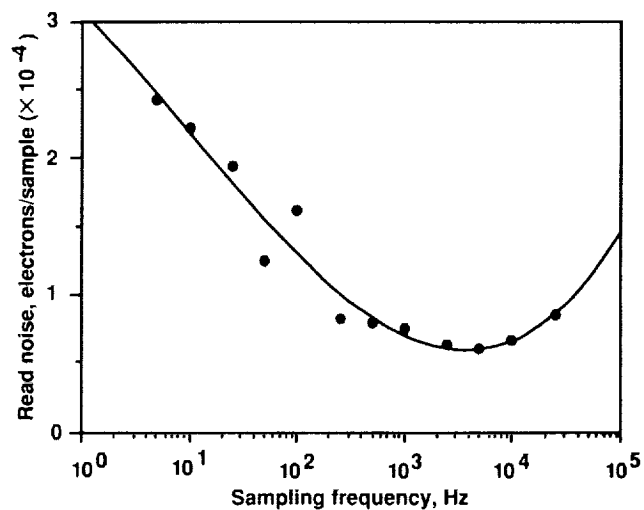


Figure 22. Dark read noise of Module 02 as a function of sampling frequency referenced to the detector output; the solid curve is the best fit to the data points. Detector temperature = 4.2 K; bias = 350 mV.

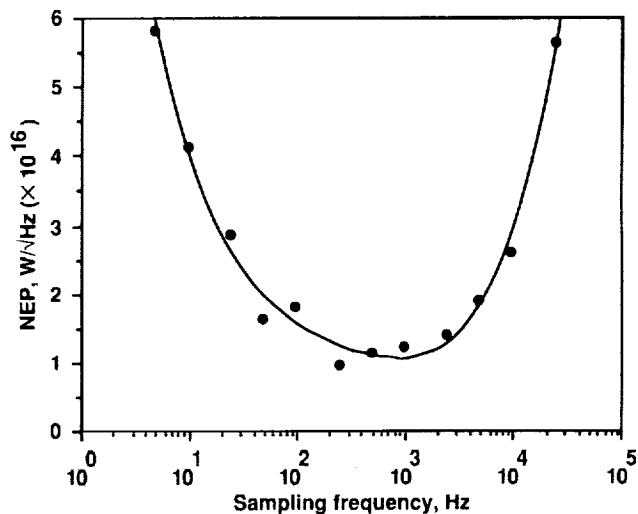


Figure 23. NEP of Module 02 as a function of sampling frequency; the solid curve is the best fit to the data points. Detector temperature = 4.2 K; bias = 350 mV.

1. Report No. NASA TM-102275		2. Government Accession No.		3. Recipient's Catalog No.	
4. Title and Subtitle Performance of Multiplexed Ge:Ga Detector Arrays in the Far Infrared				5. Report Date October 1990	
				6. Performing Organization Code	
7. Author(s) Jam Farhoomand (Sterling Federal Systems, Inc., Palo Alto, California) and Craig McCreight				8. Performing Organization Report No. A-90053	
				10. Work Unit No. 506-45-31	
9. Performing Organization Name and Address Ames Research Center Moffett Field, CA 94035-1000				11. Contract or Grant No.	
				13. Type of Report and Period Covered Technical Memorandum	
12. Sponsoring Agency Name and Address National Aeronautics and Space Administration Washington, DC 20546-0001				14. Sponsoring Agency Code	
15. Supplementary Notes Point of Contact: Craig McCreight, Ames Research Center, MS 244-10, Moffett Field, CA 94035-1000 (415) 604-6549 or FTS 464-6549					
16. Abstract The performance of two multielement, multiplexed Ge:Ga linear arrays under low-background conditions has been investigated. The on-focal-plane switching is accomplished by MOSFET switches, and the integrated charge is made available through MOSFET source followers. The tests were conducted at 106 μm , and the radiation on the detectors was confined to a spectral window 1.25 μm wide using a stack of cold filters. At 4.2 K, the highest responsivity was 584 A/W, the noise equivalent power was 1.0×10^{-16} W/ $\sqrt{\text{Hz}}$, and the read noise was 6100 electrons/sample. A detailed description of the test setup and procedure is presented. <i>... 100 W/ sqrt Hz of Hz.</i>					
17. Key Words (Suggested by Author(s)) Integrated arrays Far infrared detector Focal plane electronics Ge:Ga detector				18. Distribution Statement Unclassified-Unlimited Subject Category - 88	
19. Security Classif. (of this report) Unclassified		20. Security Classif. (of this page) Unclassified		21. No. of Pages 26	
				22. Price A03	

